HHS Public Access

Author manuscript

Biomaterials. Author manuscript; available in PMC 2019 April 09.

Published in final edited form as:

Biomaterials. 2018 November ; 182: 279–288. doi:10.1016/j.biomaterials.2018.08.028.

Layer-by-layer Nanofiber-Enabled Engineering of Biomimetic Periosteum for Bone Repair and Reconstruction

Tao Wang[1], **Yuankun Zhai**[1], **Marc Nuzzo**[1], **Xiaochuan Yang**[1], **Yunpeng Yang**[1], and **Xinping Zhang**[1]

[1]Center for Musculoskeletal Research, University of Rochester, School of Medicine and Dentistry, Rochester, NY 14642

Abstract

Periosteum plays an indispensable role in bone repair and reconstruction. To recapitulate the remarkable regenerative capacity of periosteum, a biomimetic tissue-engineered periosteum (TEP) was constructed via layer-by-layer bottom-up strategy utilizing polycaprolactone (PCL), collagen, and nano-hydroxyapatite composite nanofiber sheets seeded with bone marrow stromal cells (BMSCs). When combined with a structural bone allograft to repair a 4mm segmental bone defect created in the mouse femur, TEP restored donor-site periosteal bone formation, reversing the poor biomechanics of bone allograft healing at 6 weeks post-implantation. Further histologic analyses showed that TEP recapitulated the entire periosteal bone repair process, as evidenced by donor-dependent formation of bone and cartilage, induction of distinct $CD31^{high}$ type H endothelium, reconstitution of bone marrow and remodeling of bone allografts. Compared to nanofiber sheets without BMSC seeding, TEP eliminated the fibrotic tissue capsule elicited by nanofiber sheets, leading to a marked improvement of osseointegration at the compromised periosteal site. Taken together, our study demonstrated a novel layer-by-layer engineering platform for construction of a versatile biomimetic periosteum, enabling further assembly of a multi-component and multifunctional periosteum replacement for bone defect repair and reconstruction.

Graphical Abstract

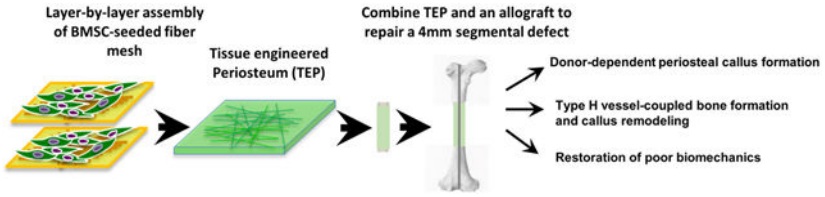

Keywords

tissue engineered periosteum; angiogenesis; nanofibers; layer-by-layer assembly

Corresponding author contact information: Dr. Xinping Zhang, The Center for Musculoskeletal Research, University of Rochester Medical Center, 601 Elmwood Avenue, Rochester, NY 14642, USA, Xinping_Zhang@URMC.rochester.edu.

1. INTRODUCTION

Repair of large segmental bone defects remains a significant challenge due to the lack of grafting materials that can match the biological and mechanical performances of a structural bone autograft. Previous studies have attributed the regenerative capacity of autografts to periosteum, which accounts for about 70% of bone and cartilage formation at the initiation of autograft healing [1, 2]. Periosteal stripping is known to be associated with a high incidence of bone nonunion, whereas preservation of periosteum or use of a periosteum tube graft significantly improves bone graft incorporation and bone defect reconstruction [3-5].

Based on the compelling clinical and experimental evidence of an indispensable role of periosteum in repair and reconstruction, a tissue engineering approach that combines structural bone allograft with functional periosteum for repair and reconstruction of large segmental bone defects has been proposed [1, 2, 6, 7]. A series of studies from our laboratory and others have shown that combining osteogenic progenitors and periosteal signaling molecules in a tissue engineering construct significantly enhances bone graft healing and incorporation [7-15]. However, despite a varied degree of success in small animal models, a complete recapitulation of the periosteum-dependent repair has not yet been reported. The fate of donor cells and the contribution of host cells to graft repair remain poorly understood. Challenges remain as to how to control bone formation along the graft surface to maximize cortical bone union, and how to induce uniform bone formation, graft remodeling and revascularization by incorporation of bioactive molecules and relevant cell populations into fabrication.

Periosteum can be divided into multiple layers, including an inner osteogenic cambium layer and an outer fibrous layer. The latter can be loosely separated into a fibrotic zone consisting mainly of collagen bundles with interspersed fibroblasts, and a substratum rich in blood vessels, neural networks and stem cells [16-19]. To simulate the highly organized periosteum and its function, here we demonstrated a novel approach utilizing composite electrospun nanofiber sheets made from polycaprolactone, collagen and nano-hydroxylapatite to construct a biomimetic periosteum for bone defect repair and reconstruction. The versatility of electrospun fiber sheets in mimicking extracellular matrix (ECM) [20-23] and the benefits of high surface-to-volume ratio fibrous matrices for cell attachment, drug loading, and mass transport [24, 25] enable the construction of a flexible tissue membrane that can fit bone of any size and shape. To overcome the limitations of nanofibrous sheets in cellular infiltration and vascular ingrowth, we further adopted a layer-by-layer assembly strategy [26], which has been successfully used in a number of tissue engineering applications to facilitate uniform cell seeding and complex tissue construction [27-32].

The goal of our current study was to validate the nanofiber-enabled layer-by-layer assembly strategy as a novel tissue-engineering platform for construction of a multilayered and multifunctional periosteum for bone defect repair and reconstruction. To this end, composite nanofiber sheets seeded with BMSCs were assembled into a flexible tissue membrane and subsequently used to wrap around a structural bone allograft to repair a 4mm segmental bone defect created in a murine model. Our data demonstrated that the engineered

periosteum recapitulated the entire intramembraneous and endochondral bone repair, leading to a marked improvement of bone allograft healing and incorporation.

2. MATERIALS AND METHODS

2.1. Experimental Animals.

All *in vivo* experiments were performed using adult 8–12 week old animals housed in pathogen-free, temperature and humidity controlled facilities with a 12 hour day-night cycle in the vivarium at the University of Rochester Medical Center. All cages contained wood shavings, bedding and a cardboard tube for environmental enrichment. All experimental procedures were reviewed and approved by the University Committee on Animal Resources. General anesthesia, and analgesia procedures were performed based on the mouse formulary provided by the University Committee on Animal Resources. The animals' health status was monitored throughout the experiments by experienced veterinarians according to the Guide for the Care and Use of Laboratory Animals outlined by the National Institute of Health.

The global GFP transgenic mice and the immunodeficient NOD.CB17-*Prkdc*^{scid}/J (NOD/SCID) mice were purchased from the Jackson Laboratory (Bar Harbor, Maine) and were used as recipients for all grafts. The Osterix-RFP^{Cherry} reporter mice [33], which label all osteoblastic lineages with cherry red fluorescence protein (RFP^{cherry}) were kindly provided by Dr. Peter Maye at the University of Connecticut Heath Science Center. The immunodeficient NOD/SCID;OSX-RFP^{cherry} mice were established by backcrossing OSX-RFP^{cherry} mice with NOD/SCID mice for more than eight generations. In these mice, RFP could only be detected in mature osteoblasts and osteocytes in bone tissue. The immunodeficiency of NOD/SCID-OSX-RFP^{cherry} mice was confirmed by the lack of T and B cells in peripheral blood via fluorescence-activated cell sorting (FACS). Tail genomic DNA preparations were used to determine the genotypes of each mouse strain using polymerase chain reaction (PCR).

2.2. Fabrication of PCL/Collagen/HAp composite nanofibrous mesh.

Polycaprolactone 8% (w/v) (PCL, SigmaAldrich, St. Louis, MO) and Collagen type I 8% (w/v) (Elastin Products, Owensville, MI) solution were prepared by dissolving in 1,1,1,3,3,3,-isopropanol (HFIP, Oakwood Products, New Orleans, Louisiana) respectively and then mixed at a volume ratio of 3:1. Nano hydroxyapatite (HAp, M K Impex Corp. Missisauga, ON, Canada) was suspended in HFIP (8% w/v) by stirring overnight and treated with ultrasound bath to achieve better suspension prior mixing with the PCL/Collagen (3:1). The ratio of PCL:Collagen:HAp is 3:1:2. Electrospinning was performed at a feeding speed of 10 μL/min by a syringe pump (Chemyx Incorporation, Houston, TX) and a 15 kV voltage power supply (Gamma High Voltage Research, Ormond Beach, FL) with a distance of 10 cm between needle and collector. Composite nanofibrous sheets were collected onto circular stainless-steel wire loops for further cell seeding and handling. Fiber meshes were prepared in a UV irradiated cabinet without any airflow. Prior to cell seeding, the fiber meshes were further soaked in isopropanol for 20 min, followed by multiple washes with PBS and culture medium. The composite fiber mesh was examined by Scanning Electron Microscope (SEM) and show randomly oriented non-woven fibers with a mean diameter of ~600nm (Fig. 1A).

2.3. Assembly of 3D cell/scaffold TEP constructs.

Bone marrow cells were isolated as previously described [34] from 8-12 weeks old transgenic mice engineered to express GFP ubiquitously. Briefly, cells were flushed from marrow cavity by slow injection of α-MEM at one end of the bone using a sterile 21-gauge needle. The marrow suspension was dispersed gently by pipetting several times to obtain a single cell suspension. The cell suspension was further filtered through a 70μm cell strainer (Falcon) to remove debris. About 5×10^6 freshly isolated bone marrow cells were seeded on each sterile electrospun fibrous sheet in 12-well plates and cultured in alpha-MEM media containing 15% fetal bovine serum (SigmaAldrich, St. Louis, MO) for 10 days with change of media every two days. Osteogenic differentiation media containing 50 μg/mL ascorbic acid (SigmaAldrich, St. Louis, MO), 5mM β-glycerophosphate (SigmaAldrich, St. Louis, MO), and 10% FBS in alpha-MEM was added at day 10 and cultured for an additional 11 days with medium change every two days. BMSC-seeded fiber sheets (20 layers) were stacked layer-by-layer via a custom-made metal clip to form a flexible membranous tissue construct (~200 μm). The constructs were cultured overnight in osteogenic media prior to transplantation.

2.4. Multiphoton laser scanning microscopy (MPLSM) to evaluate TEP construct and histology tissue sections.

An Olympus FV1000-AOM multiphoton imaging system, equipped with a Titanium:Sapphire laser, a C-Apochromat 10X/0.45(Zeiss), and a 25X/1.05 (Olympus) water immersion objectives, was used for imaging 3D tissue construct and thick tissue sections obtained from mouse femurs. Images were acquired at 512×512 pixels, 0.2 ms pixel dwell with the laser tuned to 780nm. The fluorescence of GFP, RFP and second harmonic signals (SHG) were collected with a 517/23-nm, a 605/25-nm and a 390/20-nm bandpass filters (Semrock), respectively. The 2D slice viewing and 3D reconstruction of the defect were conducted using Amira image analysis software (Visage Imaging, Berlin, Germany). Collagen matrix deposition in multilayered tissue constructs was evaluated via SHG as previously described[35]. Fluorescently labeled donor and host cell contribution to bone formation was evaluated via MPLSM using 25μm thick frozen bone tissue sections [34].

2.5. Surgical procedures for segmental femoral bone allograft model.

A 4mm segmental femoral bone graft transplantation model was used to evaluate the efficacy of tissue-engineered periosteum in reconstruction of long bone defect repair [1, 7, 13]. Briefly, mice were anesthetized via intraperitoneal injection with a combination of Ketamine and Xylazine. A transverse unilateral osteotomy was performed to remove a 4 mm femoral diaphyseal shaft using a bone saw. A devitalized allograft or a devitalized allograft wrapped with nanofiber sheets with or without BMSC-seeding was used to repair the defect. The grafts were secured by a 22-gauge metal pin placed through the intramedullary marrow cavity. Allografts were prepared from an outbred strain of FVB and washed extensively with phosphate buffered saline to remove periosteum, bone marrow cells and cell debris. The grafts were further washed with 70% ethanol, soaked in PBS containing a cocktail of penicillin and streptomycin and frozen at −80° for at least 1 week. Live autografts with intact periosteum were used as a control group in some experiments to illustrate the

difference between autograft and allograft healing in mice. To perform autograft surgery, a 4mm diaphyseal bone segment was removed from mouse femur and then placed immediately back to repair the same sized defect. During the postoperative period, pain was relieved by a subcutaneous administration of butamorphine (Pfizer Animal Health; 5 mg/kg twice daily for 2 days). TEP was cut into 4mm strips. Each strip was used to wrap around a 4mm allograft. Excessive membrane was removed to ensure direct contact between the ends of the host bone and donor bone at the junctions. A silk suture was used to keep TEP in direct contact with allograft during surgery and was subsequently removed before wound closure.

2.6. Experimental animal groups:

Based on our prior experience with the murine allograft model, which demonstrates poor graft integration and biomechanics at week 6 post-surgery [7, 12], we chose week 6 post-surgery to conduct MicroCT analyses and biomechanical testing. A total of 24 mice in 4 groups (allograft, allograft with fibers, allograft with TEP and autograft, n=6) were included in the MicroCT analyses. These same samples were used for biomechanical testing to determine the functional integration of the allograft with host bone. To track donor cell fate and bone graft healing over time, histologic and immunofluorescent analyses were performed at week 3, 5 and 7 post-surgery in TEP treated samples. At least three mice per group were used for evaluation. Histomorphometric analyses were conducted in 4 groups of samples harvested at week 5 post-surgery (allograft, allograft with fibers, allograft with TEP and autograft, n=4).

2.7. Evaluation of femoral allograft healing by MicroCT.

Samples were scanned by ScancoVivaCT 40 system (Scanco Medical AG, Bassersdorf, Switzerland) at 12.5-micron isotropic resolution. Images were reconstructed to allow 3-dimensional structural rendering of the calluses at a standardized threshold corresponding to 750 mgHA/cm^3 based on a phantom of known HA concentrations. To evaluate bone formation, contour lines were drawn in the 2-dimensional slice images to exclude the allograft and the old host cortical bone. New bone volume on the surface of the host and donor bone, as well as in the total callus in grafted samples was calculated, respectively [1, 7].

2.8. Evaluation of femoral allograft healing via histology and fluorescence microscopy.

At the end point of the experiment, mice were perfused with 4% paraformaldehyde followed by an additional tissue fixation for 2 days. The specimens were decalcified in 10% EDTA and processed for frozen sectioning. Mid-sagittal frozen sections (20 microns thick) were stained with Hematoxylin & Eosin plus Alcian blue hematoxylin/orange G, or tartrate-resistant acidic phosphatase (TRAP) as previously described [1, 7, 13]. Tissue sections were digitalized via Olympus VS110™ Virtual Slide Scanning System (Olympus, Tokyo, Japan). Histomorphometric analyses of bone, cartilage, and fibrotic tissue formation were performed in the VisioPharm Image Analysis Software via color-based semi-manual segmentation of different tissue component of the healing callus (Hørsholm, Denmark) [36, 37]. Percentage area of bone, cartilage, bone marrow and fibrotic tissue within the area of callus were calculated to illustrate the difference among each group of samples.

2.9. Evaluation of femoral allograft healing via torsional biomechanical testing.

Following sacrifice, the tibia was isolated and cleaned of excess soft tissue. Tibias were stored at 4°C in phosphate saline buffer overnight, prior to torsional biomechanical testing. The ends of the tibias were cemented (Bosworth Company) in aluminum tube holders and tested using an EnduraTec TestBench™ system (Bose Corporation, Eden Prairie, MN). The tibias were tested at a rate of 1deg/sec, in torsion, until failure. The rotational data was converted to radians/mm to complete the torsional rigidity analysis. The ultimate torque and the torsional rigidity were determined based on the load-to-failure curve generated. The intact femurs from non-surgical NOD/SCID mice and the contralateral femurs of the surgical mice were used as controls for allografted bone in torsional biomechanical testing.

2.10. Immunofluorescent staining of blood vessels and microscopy.

Mice were perfused with 4% paraformaldehyde following surgery as previously described. The samples were treated with 3% bovine albumin in PBS containing 0.3% Triton X-100 and then stained with CD31 antibody (1:100 dilution, Biolegend, San Diego, CA) and Endomucin (Emcn) antibody (1:50 dilution, Santa Cruz Biotechnology, Santa Cruz, CA) overnight at 4°C. The samples were imaged via Olympus VS110™ Virtual Slide Scanning System (Olympus, Tokyo, Japan) or MPLSM as described above. Semi-quantitative analyses of vessel number were performed using digitized images obtained from Olympus VS110™ Virtual Slide Scanning System (Olympus, Tokyo, Japan). At least three sections per sample were used in the analyses.

2.11. Statistical analyses.

All data are shown as the mean ± standard error. Statistical analysis was analyzed by one-way ANOVA in GraphPad Prism (GraphPad Prism, San Diego, CA). A p value <0.05 following Bonferroni correction was considered statistically significant.

3. RESULTS

3.1. Assembly of multilayered TEP constructs.

BMSCs harvested from GFP transgenic mice were seeded onto the composite nanofiber sheets (Fig. 1A&B). The seeded fiber sheets were cultured for 21 days to induce bone cell differentiation (Supplemental Fig.1S). Twenty layers of BMSC-seeded fiber sheets (~2 μm/layer) were stacked layer-by-layer to form a flexible membranous tissue construct via a custom-made metal clip (Fig. 1C&D). When examined by MPLSM confocal microscopy, the construct showed GFP^+ BMSCs and rich SHG^+ collagen matrix deposition within the formed construct (Fig. 1E&F). Histologic staining further illustrated layered tissue formation (Fig. 1G) and $PicroSirius^+$ collagen matrix (Fig. 1H).

3.2. TEP restored donor site periosteal bone formation and markedly enhanced bone allograft incorporation.

The multilayered TEP constructs with or without BMSCs were wrapped around 4mm bone allografts and used to repair the same sized segmental defects created in the femurs of the immunodeficient mice. MicroCT analyses showed minimal donor-site periosteum callus at

week 6 post-transplantation in allograft alone or allograft treated with acellular fiber sheets (Fig. 2A). TEP treatment completely restored donor-site periosteal callus formation and host-graft osseointegration, similar to autograft healing. MicroCT 2D slice views further illustrated the organized multilayered bone formation around allograft and the incorporation of allograft into host bone in the TEP treated sample (Fig. 2B). Compared to allograft control, TEP treated group showed 6.2, 2.1 and 3.5-fold higher bone volume than allograft control group at the graft side, host side and in total callus, respectively (Fig. 2C, D and E, $p<0.05$, $n=6$). The fiber control group showed no significant increase in bone formation ($p>0.05$).

3.3. TEP induced donor-cell-dependent intramembraneous and endochondral bone formation at the compromised periosteal sites.

Histologic analyses were performed in samples harvested at week 5 post surgery. Alcian blue/H&E staining showed limited bone formation and poor bony union at the cortical bone junction in allograft control group (Fig. 3A1&2). Treatment with acellular nanofiber sheets induced fibrotic tissue formation around allografts, disrupting bony union (Fig. 3B1&2, # indicating fibrotic tissue). In contrast, TEP treated allograft induced multiple layers of bone and cartilage formation surrounding allograft, with more cartilage formed adjacent to the allograft surface (Fig. 3C1&2). GFP fluorescent microscopy showed donor GFP^+ cells confined within the fibrous layers of the TEP implant, confirming the donor origin of the newly formed bone and cartilage (Fig. 3C3). Compared to the autografted femurs (Fig. 3D1-2), TEP wrapped allografts showed delayed remodeling of the cartilaginous callus at the graft surface at week 5.

Histomorphometric analyses comparing percent bone, marrow, cartilage, and fibrotic tissue formation revealed that TEP treated grafts had 3.8-fold and 2.0-fold more bone than allograft alone or allograft treated with fibers at the donor periosteal site (Fig. 3E, $p<0.05$, $n=4$). The TEP group also had 4.5-fold more cartilage than the two control groups. Similar to autograft healing, TEP enhanced bone and cartilage formation in host side callus (Fig. 3E, $p<0.05$). Of note is the increased fibrotic tissue formation in the fiber control group which was found to be the highest among all four groups ($p<0.01$).

Further time course analyses were conducted in the TEP treated allografts at weeks 3, 5, and 7 post transplantation to examine the formation and remodeling of the donor site periosteal callus. Donor-dependent chondrogenesis was initiated at week 3 (Fig. 4A) and peaked at week 5 (Fig. 4B) post transplantation. By week 7, only a small amount of cartilage was identified in the callus (Fig. 4C), indicating a progressive endochondral bone formation in TEP group. Further fluorescence microscopy and CD31 staining confirmed the donor-dependent bone formation and progressive vascular invasion into donor GFP^+ callus at weeks 3, 5 and 7 (Fig. 4D-F). TRAP staining demonstrated recruitment of $TRAP^+$ osteoclasts into donor site periosteal callus (Fig. 4G-I). At a higher magnification, $TRAP^+$ osteoclasts were found along bone surface and in calcified cartilaginous tissue (Fig. 4J-N). While most osteoclasts were found closely associated with newly formed donor bone (Fig. 4L&M), $TRAP^+$ cells could also be identified along allograft bone at week 7 (Fig. 4N), indicating active remodeling of the periosteal callus and bone allografts.

3.4. TEP facilitated donor-host bone integration at the compromised periosteal sites.

The integration of donor/host callus were examined by transplanting GFP^+ BMSC-seeded TEP into an immuno-deficient NOD-$OSX^{RFPcherry}$ mouse model that marked host osteoblasts and osteocytes with red fluorescence protein. At week 7 post transplantation, abundant OSX-$cherry^+$ cells were seen at the host site callus flanking the GFP^+ donor derived callus (Fig. 5A). At a higher magnification, mixed OSX-$Cherry^+$ host and GFP^+ donor cells were found within layers of newly formed bone in between fibers (Fig. 5D&F, red arrows indicate host-derived bone and white arrows indicate donor-derived bone), suggesting joint contribution of bone formation from donor and host. At the cortical bone junction, OSX-$cherry^+$ cells were seen migrating into the donor callus along fiber layers, with host OSX^+ cells integrated into the donor callus (Fig. 5E, white arrows). OSX-cherry+ cells could also be found along allograft surface, indicating active bone formation along allograft surface (Fig. 5E&G, red arrows). Osseointegration at the cortical bone junction was evident by formation of the chimeric bone (Fig. 5G).

3.5. TEP induced distinct type H endothelium associated with endochondral bone formation at the donor periosteal sites.

$CD31^{high}Emcn^{high}$ type H vessels have recently been shown to couple with trabecular bone formation beneath growth plate during endochondral development and aging [38, 39]. To determine the vascular response associated with TEP induced angiogenesis, Endomucin (Emcn) and CD31 immunofluorescent staining were performed in all three groups of samples. As shown, the irregularly shaped $CD31^{high}Emcn^{high}$ type H vessels were found closely associated with newly formed trabecular bone in periosteal callus in all three groups of samples examined (Fig. 6, overlaying color as magenta). Compared to allograft alone or allograft treated with acellular fibers, type H vessels were found to be markedly increased in donor site periosteal callus (Fig. 6A&B vs. E&F). Compared with vessels in quiescent bone marrow where no active bone formation took place (supplemental data Fig. S2), CD31 expression was much stronger in vessels associated with bone formation, corroborating with the previous reports that suggest $CD31^{high}$ endothelium as the functional vessel type coupling with endochondral bone development whereas $Emcn^{high}$ vessels as the quiescent sinusoidal vessels in bone marrow [38, 39]. In the nanofiber only group, vessels in the fibrotic tissue on top of allografts or at cortical bone junctions were distinct from the irregular-shaped type H vessels in bone callus (Fig. 6C&D). These vessels were heterogeneous without significant morphological distinctions on tissue sections. Further examination of the samples obtained at week 3, 5 and 7 in TEP group showed that $CD31^{high}Emcn^{high}$ vessels could be identified as early as week 3 at the donor-host interface (Fig. 6G, magenta). These vessels were found invading the cartilage tissue (Fig. 6H) and forming distinctive multilayered $CD31^{high}Emcn^{high}$ type H vasculature in between layered donor-derived bone at week 5 (Fig. 6F&I). These vessels remained at active bone forming and remodeling sites within donor periosteal callus at week 7 (Fig. 6J). Of note is that among the $CD31^{high}Emcn^{high}$ large irregular shaped vessels, $CD31^{high}Emcn^{null}$ microvasculature could also be identified in bone forming callus at various stage of bone formation (Fig. 6G-I, red), indicating the $CD31^{high}$ vasculature as the key blood vessel type coupled with bone formation in repair.

Quantitative analyses were performed to examine the $CD31^{+}$ blood vessel formation in total new bone callus and the $CD31^{high}Emcn^{high}$ type H vessel formation in donor periosteal callus at week 5 post-surgery. The total vessel formation in both nanofiber treated groups was increased as compared to the allograft alone group. However, the TEP treated group showed about 2-fold more vessels than the nanofiber only group (Fig. 6K, $p<0.05$, $n=4$). Within the newly formed donor site periosteal callus, the type H vessels in TEP group were increased by 5.4 fold as compared to the other two groups (Fig. 6L, $p<0.05$, $n=4$).

3.6. TEP reversed the inferior biomechanics of bone allograft healing.

To determine the functional integration of donor and host derived bone callus, torsional biomechanical testing was performed at weeks 6 post surgery. TEP treated allografts completely reversed the inferior biomechanics of the allografted bone at weeks 6 post-surgery, restoring the maximum torque and torsional rigidity to 85% of those of the intact femurs or 81% of those of the contralateral femurs of the surgical mice (Fig. 7A&B, $p<0.05$, $n=6$). Of note is that the torsional rigidity and maximum torque in the acellular fiber-treated allografts were significantly lower than allograft control group, suggesting inferior osseointegration that was likely due to the fibrotic tissue formation induced by fiber sheets ($p<0.05$).

4. DISCUSSION

Periosteum-initiated bone graft repair is a donor progenitor cell-dependent process, in which coordinated vascular invasion and bone/cartilage formation are commenced to promote subsequent remodeling and incorporation of the donor bone grafts [1, 2]. To mimic this unique process, we developed a novel TEP construct utilizing electrospun nanofiber sheets seeded with BMSCs. When wrapped around a 4mm femoral bone allograft, engineered periosteum induced both intramembraneous and endochondral bone healing typically observed in periosteal repair. Tracking of the donor and host osteogenic cells showed that the engineered periosteum induced donor cell-dependent bone/cartilage formation, facilitating the migration of host osteoblasts along nanofiber sheet into donor implants. Donor progenitor cells underwent chondrogenic differentiation at a site where vascularity was poor (close to allograft surface), and osteoblastic differentiation at a site where vascularity was more available (close to muscle). Compared with the previous attempts at delivery of BMSCs via collagen gel foam or hydrogel [1, 12], our current biomimetic TEP demonstrated more uniform bone formation around bone allografts, leading to markedly enhanced osseointegration and a complete reversal of the inferior biomechanics of the allografted bone at 6 week post-implantation. Compared with the previously published cell sheet technology [10], our current approach demonstrated improved flexibility and versatility in construction and handling of the TEP for future clinical application.

A highly organized cellular microenvironment with proper assembly of the native ECM is critically important for survival and differentiation of the donor cells at the site of defect repair. Despite the fact that the electrospun fibers resemble the non-woven fibrous structures of ECM, the nano-scale structures of the native collagen matrix are vastly different from those of the electrospun nanofibers [35, 40]. To enhance the donor cell survival and

differentiation *in vivo*, we utilized the nanofiber sheets cultured with BMSCs for 20 days as the building blocks for engineered periosteum. Compared with other similar electrospun fiber-based 3D scaffolds, our current TEP construct included both committed bone forming progenitors and rich deposits of the native ECM produced by BMSCs, forming an ideal cellular microenvironment to support donor cell growth and differentiation *in vivo*. Tracking of the donor cell fate confirmed the sustained donor cell survival and differentiation over 7-week period *in vivo* in the layer-by-layer assembled 3D scaffolds. The beneficial effects of the native ECM in bone/cartilage engineering have been extensively published [41, 42]. Our current study demonstrated a simple strategy to optimize the performance of electrospun nanofibrous sheets in bone repair and bone tissue engineering.

Endochondral bone formation coupled with vascular invasion and callus remodeling has been the corner stone of periosteum-dependent repair and reconstruction. Utilizing immunofluorescence microscopy, in this study, we identified the unique coupling of $CD31^{high}$ type H endothelium with new bone formation in periosteal callus. Histologically, these vessels were distinct from vessels in quiescent bone marrow or in soft tissues. Implantation of TEP at the periosteal sites markedly induced the $CD31^{high}$ endothelium associated with donor-dependent endochondral bone formation. The $CD31^{high}$ type H vessels have previously been identified in metaphysis beneath the growth plate [38, 39, 43]. These vessels have relatively higher velocity perfusion as opposed to $CD31^{low}$ $Emcn^{high}$ vessels in quiescent bone marrow, and are regulated by BMP and Notch signaling pathways during development and aging [38, 39, 43]. The marked induction of type H vessels in TEP-induced periosteal callus demonstrated the strong regenerative capacity of the engineered periosteum in repair, validating our current cell-based approach for reconstruction of bony defects. The distinct morphology of the neovasculature at the site of repair further indicated that the regenerative neovasculature induced by BMSCs had distinct molecular, cellular and functional properties. A deeper understanding of the vessel types associated with periosteum-dependent repair could yield useful information on molecular control of angiogenesis, aiding in construction of vascularized engineered constructs for improved repair and reconstruction.

It is worth noting that our current success remains as the first step for construction of a biomimetic periosteum for repair. Different from other bone tissue engineering applications which are aimed at regeneration of a permanent bone tissue for restoring function, our current approach is directed at developing a periosteum mimetic capable of recapitulating the early stage of bone healing process to enhance the recruitment of host progenitor cells for improved repair and remodeling of the donor bone grafts. Comparing with bone autograft healing, TEP-induced bone formation and callus remodeling were significantly delayed. Further modifications by delivery of adequate periosteal signals and osteogenic/angiogenic cells are essential to improve the performance of the engineered constructs. To this end, the layer-by-layer bottom-up strategy offers an effective means for spatiotemporally controlled integration of periosteal signals as well as osteogenic/angiogenic cells into the engineered constructs. Lastly, our current approach utilized immunodeficient animals to simulate autologous transplantation. Future studies utilizing large animal models that permit harvesting sufficient number of autologous cells for transplantation will determine the translatability of this approach to human.

5. CONCLUSIONS

Collectively, our current study demonstrates a novel tissue-engineering strategy for construction of a flexible biomimetic periosteum for bone defect repair and reconstruction. The engineered flexible periosteum can combine with various natural and synthetic structural bone graft materials to repair defects of any size and shape. The layer-by-layer strategy further permits controlled insertion of multiple functional components, offering added flexibility, versatility and plasticity to the engineered periosteum. With the additional advantage for modification and tuning of each cellular layer to mimic the specific microenvironment of periosteum, the strategy could offer an effective platform for construction of a biomimetic periosteum replacement that recapitulates the unique cellular, molecular, structural and functional properties of the native periosteum.

Supplementary Material

Refer to Web version on PubMed Central for supplementary material.

ACKNOWLEDGEMENTS:

We thank Michael Thullen for MicroCT scanning and related imaging analyses. This study is supported by grants from the National Institutes of Health (RO1AR067859, RO1DE019902, R21DE02656, P30AR061307).

REFERENCES:

[1]. Zhang X, Xie C, Lin AS, Ito H, Awad H, Lieberman JR, et al. Periosteal progenitor cell fate in segmental cortical bone graft transplantations: implications for functional tissue engineering. J Bone Miner Res. 2005;20:2124–37. [PubMed: 16294266]

[2]. Zhang X, Awad HA, O'Keefe RJ, Guldberg RE, Schwarz EM. A perspective: engineering periosteum for structural bone graft healing. Clin Orthop Relat Res. 2008;466:1777–87. [PubMed: 18509709]

[3]. Lozada-Gallegos AR, Letechipia-Moreno J, Palma-Lara I, Montero AA, Rodriguez G, Castro-Munozledo F, et al. Development of a bone nonunion in a noncritical segmental tibia defect model in sheep utilizing interlocking nail as an internal fixation system. J Surg Res. 2013;183:620–8. [PubMed: 23535114]

[4]. Knothe Tate ML, Ritzman TF, Schneider E, Knothe UR. Testing of a new one-stage bone-transport surgical procedure exploiting the periosteum for the repair of long-bone defects. J Bone Joint Surg Am. 2007;89:307–16. [PubMed: 17272445]

[5]. Knothe Tate ML, Dolejs S, McBride SH, Matthew Miller R, Knothe UR. Multiscale mechanobiology of de novo bone generation, remodeling and adaptation of autograft in a common ovine femur model. J Mech Behav Biomed Mater. 2011;4:829–40. [PubMed: 21616464]

[6]. Tiyapatanaputi P, Rubery PT, Carmouche J, Schwarz EM, O'Keefe RJ, Zhang X. A novel murine segmental femoral graft model. J Orthop Res. 2004;22:1254–60. [PubMed: 15475206]

[7]. Xie C, Reynolds D, Awad H, Rubery PT, Pelled G, Gazit D, et al. Structural bone allograft combined with genetically engineered mesenchymal stem cells as a novel platform for bone tissue engineering. Tissue Eng. 2007;13:435–45. [PubMed: 17518596]

[8]. Zou XH, Cai HX, Yin Z, Chen X, Jiang YZ, Hu H, et al. A novel strategy incorporated the power of mesenchymal stem cells to allografts for segmental bone tissue engineering. Cell Transplant. 2009;18:433–41. [PubMed: 19622230]

[9]. Zhao L, Zhao J, Wang S, Wang J, Liu J. Comparative study between tissue-engineered periosteum and structural allograft in rabbit critical-sized radial defect model. J Biomed Mater Res B Appl Biomater. 2011;97:1–9. [PubMed: 21290569]

[10]. Long T, Zhu Z, Awad HA, Schwarz EM, Hilton MJ, Dong Y. The effect of mesenchymal stem cell sheets on structural allograft healing of critical sized femoral defects in mice. Biomaterials. 2014.

[11]. Gamie Z, Tran GT, Vyzas G, Korres N, Heliotis M, Mantalaris A, et al. Stem cells combined with bone graft substitutes in skeletal tissue engineering. Expert Opin Biol Ther. 2012;12:713–29. [PubMed: 22500826]

[12]. Hoffman MD, Xie C, Zhang X, Benoit DS. The effect of mesenchymal stem cells delivered via hydrogel-based tissue engineered periosteum on bone allograft healing. Biomaterials. 2013;34:8887–98. [PubMed: 23958029]

[13]. Huang C, Tang M, Yehling E, Zhang X. Overexpressing sonic hedgehog peptide restores periosteal bone formation in a murine bone allograft transplantation model. Mol Ther. 2014;22:430–9. [PubMed: 24089140]

[14]. Ito H, Koefoed M, Tiyapatanaputi P, Gromov K, Goater JJ, Carmouche J, et al. Remodeling of cortical bone allografts mediated by adherent rAAV-RANKL and VEGF gene therapy. Nat Med. 2005;11:291–7. [PubMed: 15711561]

[15]. Koefoed M, Ito H, Gromov K, Reynolds DG, Awad HA, Rubery PT, et al. Biological effects of rAAV-caAlk2 coating on structural allograft healing. Mol Ther. 2005;12:212–8. [PubMed: 16043092]

[16]. Colnot C, Zhang X, Knothe Tate ML. Current insights on the regenerative potential of the periosteum: molecular, cellular, and endogenous engineering approaches. J Orthop Res. 2012;30:1869–78. [PubMed: 22778049]

[17]. Knothe Tate ML, Yu NY, Jalilian I, Pereira AF, Knothe UR. Periosteum mechanobiology and mechanistic insights for regenerative medicine. BoneKEy reports. 2016;5:857. [PubMed: 27974968]

[18]. Dwek JR. The periosteum: what is it, where is it, and what mimics it in its absence? Skeletal Radiol. 2010;39:319–23. [PubMed: 20049593]

[19]. Squier CA, Ghoneim S, Kremenak CR. Ultrastructure of the periosteum from membrane bone. J Anat. 1990;171:233–9. [PubMed: 2081707]

[20]. Subramony SD, Dargis BR, Castillo M, Azeloglu EU, Tracey MS, Su A, et al. The guidance of stem cell differentiation by substrate alignment and mechanical stimulation. Biomaterials. 2013;34:1942–53. [PubMed: 23245926]

[21]. Dahlin RL, Kasper FK, Mikos AG. Polymeric nanofibers in tissue engineering. Tissue Eng Part B Rev. 2011;17:349–64. [PubMed: 21699434]

[22]. Liu W, Thomopoulos S, Xia Y. Electrospun nanofibers for regenerative medicine. Advanced healthcare materials. 2012;1:10–25. [PubMed: 23184683]

[23]. Baker BM, Handorf AM, Ionescu LC, Li WJ, Mauck RL. New directions in nanofibrous scaffolds for soft tissue engineering and regeneration. Expert review of medical devices. 2009;6:515–32. [PubMed: 19751124]

[24]. Sill TJ, von Recum HA. Electrospinning: applications in drug delivery and tissue engineering. Biomaterials. 2008;29:1989–2006. [PubMed: 18281090]

[25]. Pham QP, Sharma U, Mikos AG. Electrospinning of polymeric nanofibers for tissue engineering applications: a review. Tissue Eng. 2006;12:1197–211. [PubMed: 16771634]

[26]. Yang X, Shah JD, Wang H. Nanofiber enabled layer-by-layer approach toward three-dimensional tissue formation. Tissue Eng Part A. 2009;15:945–56. [PubMed: 18788981]

[27]. Beachley V, Katsanevakis E, Zhang N, Wen X. A novel method to precisely assemble loose nanofiber structures for regenerative medicine applications. Advanced healthcare materials. 2013;2:343–51. [PubMed: 23184622]

[28]. Chen X, Fu X, Shi JG, Wang H. Regulation of the osteogenesis of pre-osteoblasts by spatial arrangement of electrospun nanofibers in two- and three-dimensional environments. Nanomedicine : nanotechnology, biology, and medicine. 2013;9:1283–92.

[29]. Croisier F, Atanasova G, Poumay Y, Jerome C. Polysaccharide-coated PCL nanofibers for wound dressing applications. Advanced healthcare materials. 2014;3:2032–9. [PubMed: 25263074]

[30]. Hong JK, Madihally SV. Three-dimensional scaffold of electrosprayed fibers with large pore size for tissue regeneration. Acta Biomater. 2010;6:4734–42. [PubMed: 20620245]

[31]. Shalumon KT, Chennazhi KP, Nair SV, Jayakumar R. High thick layer-by-layer 3D multiscale fibrous scaffolds for enhanced cell infiltration and it's potential in tissue engineering. Journal of biomedical nanotechnology. 2013;9:2117–22. [PubMed: 24266265]

[32]. Xin S, Li X, Wang Q, Huang R, Xu X, Lei Z, et al. Novel layer-by-layer structured nanofibrous mats coated by protein films for dermal regeneration. Journal of biomedical nanotechnology. 2014;10:803–10. [PubMed: 24734533]

[33]. Strecker S, Fu Y, Liu Y, Maye P. Generation and characterization of Osterix-Cherry reporter mice. Genesis. 2012.

[34]. Huang C, Ness VP, Yang X, Chen H, Luo J, Brown EB, et al. Spatiotemporal Analyses of Osteogenesis and Angiogenesis via Intravital Imaging in Cranial Bone Defect Repair. J Bone Miner Res. 2015;30:1217–30. [PubMed: 25640220]

[35]. Lyu S, Huang C, Yang H, Zhang X. Electrospun fibers as a scaffolding platform for bone tissue repair. J Orthop Res. 2013;31:1382–9. [PubMed: 23580466]

[36]. Dhillon RS, Zhang L, Schwarz EM, Boyce BF, Xie C. The murine femoral bone graft model and a semiautomated histomorphometric analysis tool. Methods Mol Biol. 2014;1130:45–59. [PubMed: 24482164]

[37]. Zhang L, Chang M, Beck CA, Schwarz EM, Boyce BF. Analysis of new bone, cartilage, and fibrosis tissue in healing murine allografts using whole slide imaging and a new automated histomorphometric algorithm. Bone research. 2016;4:15037. [PubMed: 26816658]

[38]. Ramasamy SK, Kusumbe AP, Schiller M, Zeuschner D, Bixel MG, Milia C, et al. Blood flow controls bone vascular function and osteogenesis. Nature communications. 2016;7:13601.

[39]. Ramasamy SK, Kusumbe AP, Wang L, Adams RH. Endothelial Notch activity promotes angiogenesis and osteogenesis in bone. Nature. 2014;507:376–80. [PubMed: 24647000]

[40]. Barnes CP, Sell SA, Boland ED, Simpson DG, Bowlin GL. Nanofiber technology: designing the next generation of tissue engineering scaffolds. Adv Drug Deliv Rev. 2007;59:1413–33. [PubMed: 17916396]

[41]. Zhang W, Zhu Y, Li J, Guo Q, Peng J, Liu S, et al. Cell-Derived Extracellular Matrix: Basic Characteristics and Current Applications in Orthopedic Tissue Engineering. Tissue Eng Part B Rev. 2016;22:193–207. [PubMed: 26671674]

[42]. Chen XD, Dusevich V, Feng JQ, Manolagas SC, Jilka RL. Extracellular matrix made by bone marrow cells facilitates expansion of marrow-derived mesenchymal progenitor cells and prevents their differentiation into osteoblasts. J Bone Miner Res. 2007;22:1943–56. [PubMed: 17680726]

[43]. Kusumbe AP, Ramasamy SK, Adams RH. Coupling of angiogenesis and osteogenesis by a specific vessel subtype in bone. Nature. 2014;507:323–8. [PubMed: 24646994]

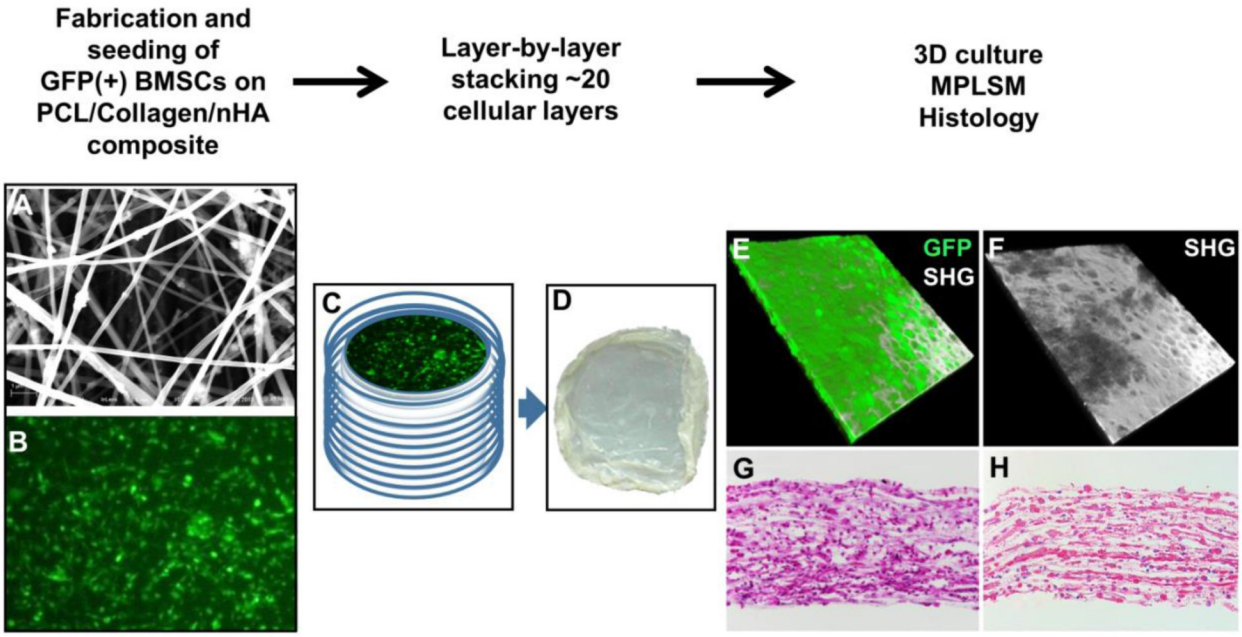

Figure 1. Layer-by-layer assembly of electrospun nanofibrous TEP construct.

Schematic illustration of fabrication (A), seeding (B), and assembly of the 3D nanofiber/cell construct (C). Gross appearance of the flexible tissue membrane (D). MPLSM images show stacked 3D construct with GFP^+ BMSCs (E) embedded in rich SHG^+ collagen matrix (F). GFP, green; SHG, white. Histologic H&E (G) and Picrosirius Red staining (H) show a multi-layered cellular construct at day 2 following assembly.

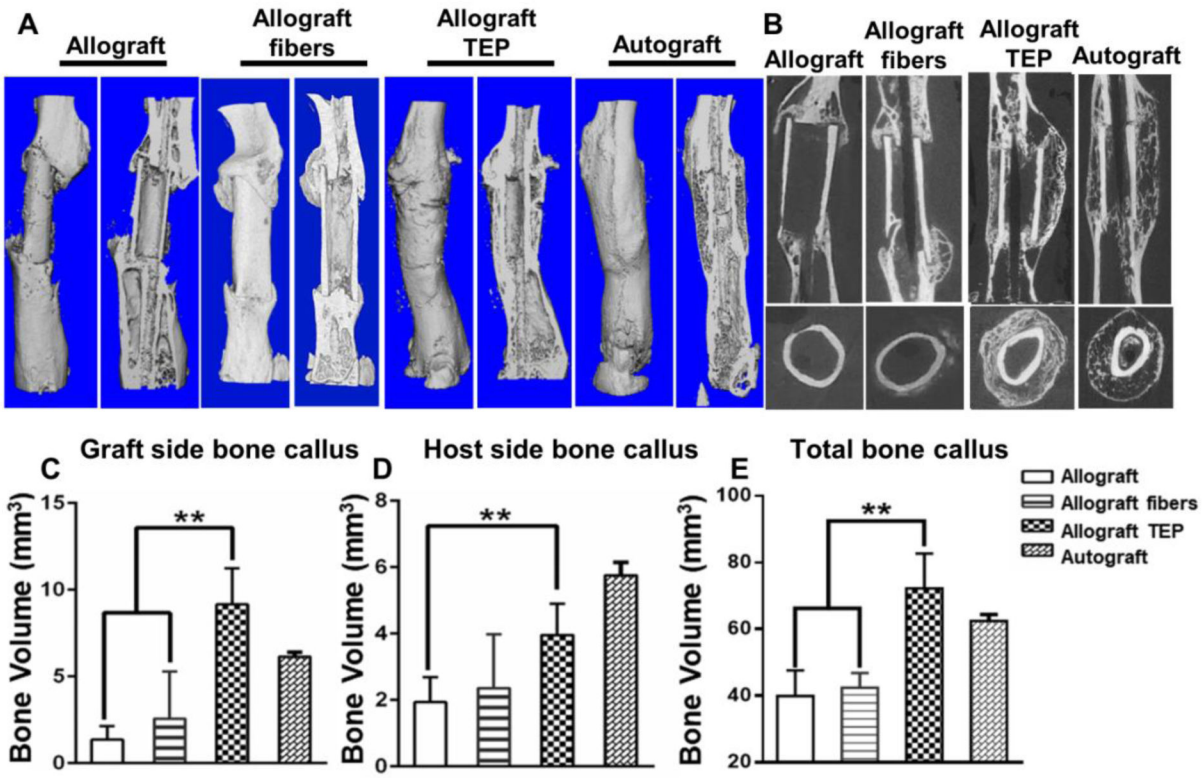

Figure 2. TEP restored donor site periosteal callus formation and enhanced donor allograft incorporation in repair of a 4mm segmental bone defect.

Representative MicroCT 3D images of autograft and allograft with or without TEP treatment 6 weeks post-surgery (A). Longitudinal and cross-sectional MicroCT 2D slice views illustrate organized multilayered periosteal bone formation in TEP treated sample as opposed to the other groups (B). Volumetric MicroCT analyses of new bone in donor (C), host (D) and total callus (E). n=6, $p<0.05$

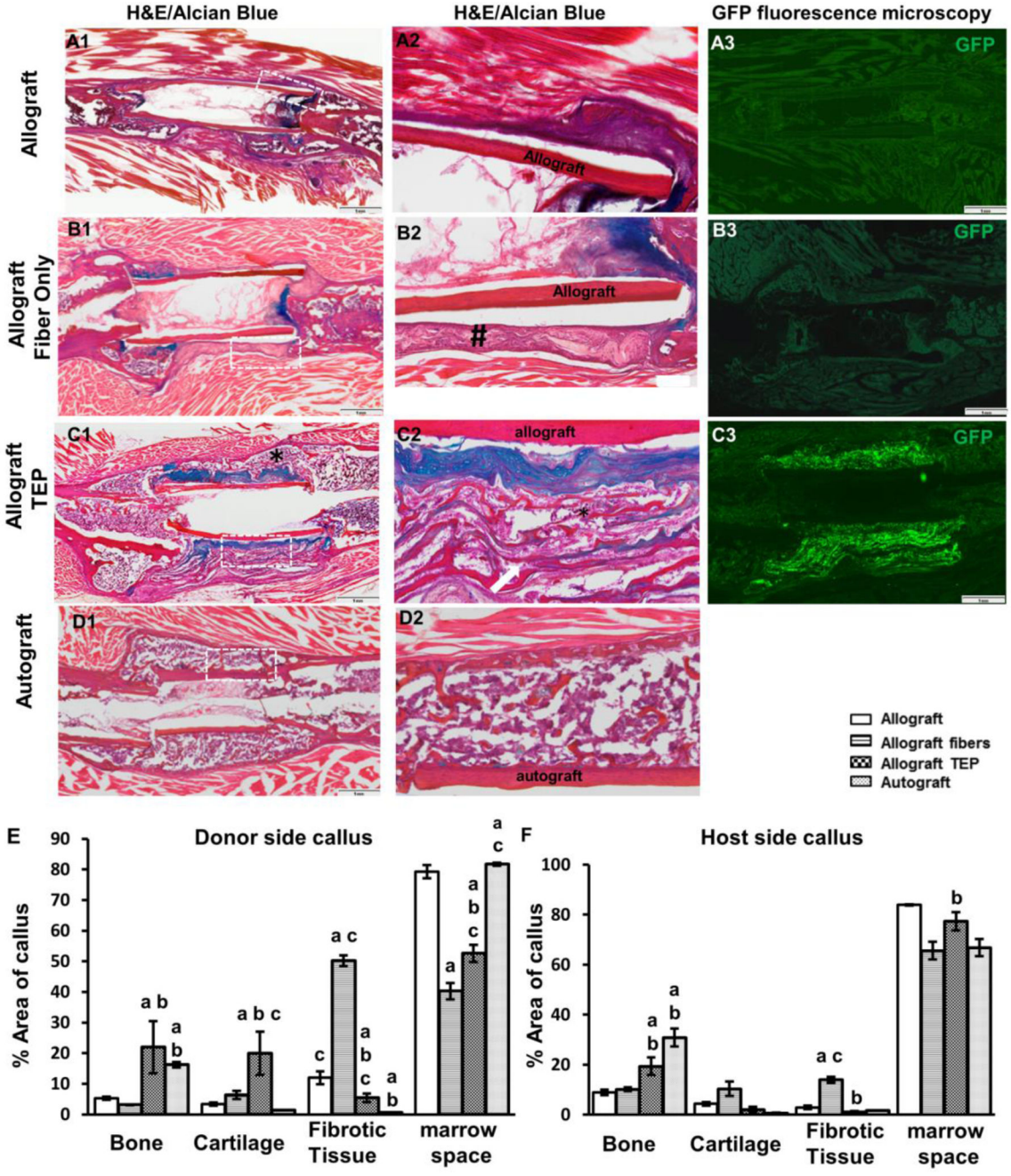

Figure 3. TEP induced donor-dependent bone/cartilage formation in femoral allograft healing.

Histology of Alcian Blue/H&E staining and GFP fluorescence microscopy of allograft (A1-3), allograft with fibers (B1-3), allograft with TEP (C1-3) and autograft (D1-2) at weeks 5 post-surgery. Scale bar=1mm. Boxed regions in A1, B1, C1 and D1 are illustrated in A2, B2, C2 and D2, respectively. Of note is the fibrotic capsule around bone allograft in fiber only group (indicated by # in B2) and the reconstituted bone marrow in TEP treated group (indicated by * in C1 and C2). Quantitative histomorphometric analyses show the percent of bone, cartilage, fibrotic tissue and bone marrow space in donor (E) and host periosteal callus

(F). a, $p<0.05$ *versus* allograft; b, $p<0.05$ *versus* allograft with fibers; c, $p<0.05$ *versus* autograft. n=4.

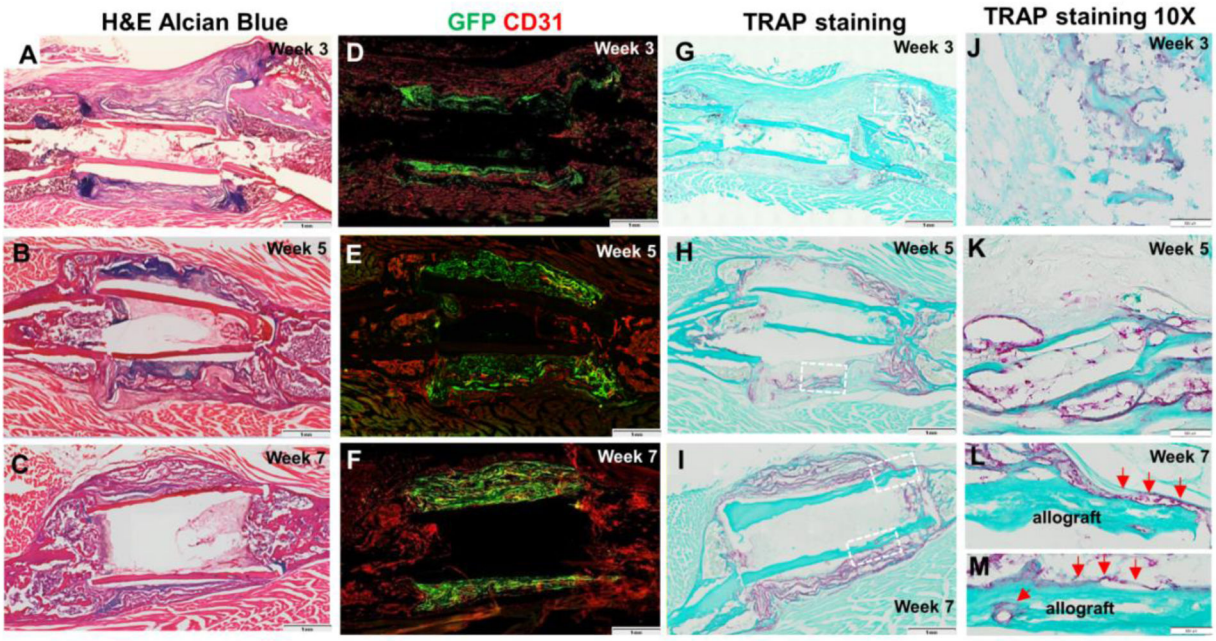

Figure 4. Time course analyses of TEP induced periosteal bone formation.

GFP^+ BMSC-seeded TEP constructs were used to wrap around allografts and implanted in 4mm femoral defects created in mice. Samples were harvested at week 3, 5 and 7 post-surgery. H&E Alcian Blue staining of the tissue sections (A-C) shows progressive endochondral bone formation at the periosteal sites. Fluorescent image of CD31 stained tissue sections shows progressive vascular invasion into donor side periosteal implants (D-F). TRAP staining shows progressive osteoclast recruitment into donor periosteal callus at week 3, 5 and 7 (G-I). Scale bar=1mm. Boxed regions in G, H, I at 40x magnification show $TRAP^+$ osteoclasts at week 3 at the interface of endochondral bone formation (J) and on new bone surface (K), week 5 on the surface of donor bone (L), and week 7 along newly formed multilayered bone surface (M). $TRAP^+$ osteoclasts can be found along allograft surface at week 7 (N, red arrows). Scar bar=20μm.

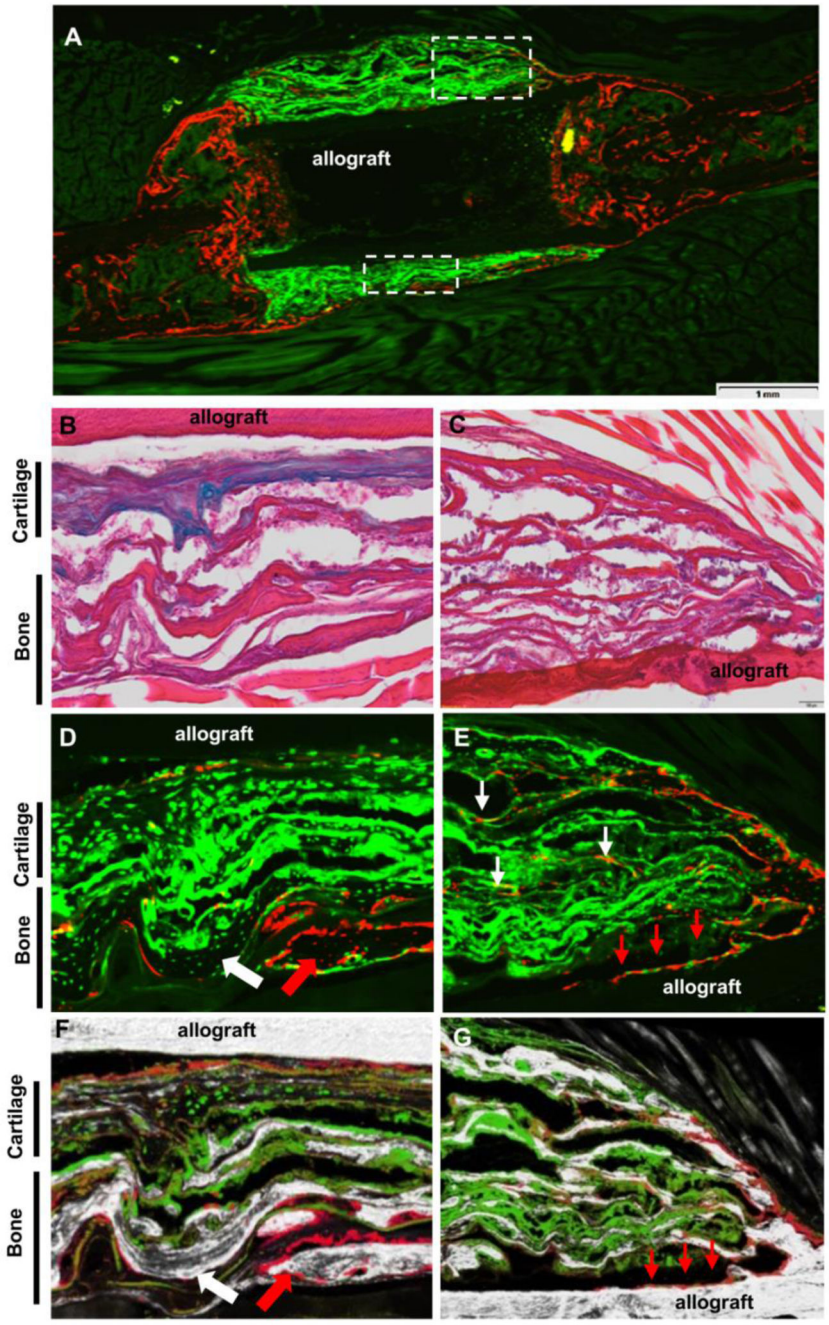

Figure 5. Donor/host contribution to engineered periosteal callus in femoral allograft healing.

GFP^{+} BMSC-seeded TEP was implanted into an immunodeficient NOD-OSX^{RFPcherry} mouse. Representative fluorescent images of the grafted femur at 7 weeks post-implantation (A). Scale bar=1mm. Boxed regions at mid-shaft (B, D, F) and cortical junction (C, E, G) are shown at a higher magnification without bone/SHG (D&E) or with bone/SHG (F&G). Chimeric bone derived from donor (green, white arrow) and host (red, red arrow) is illustrated (D and F). Note that host OSX-cherry^{+} osteoblasts migrating along fiber layers (white arrows in E) and allograft surface (red arrows in E and G) at the cortical bone junction.

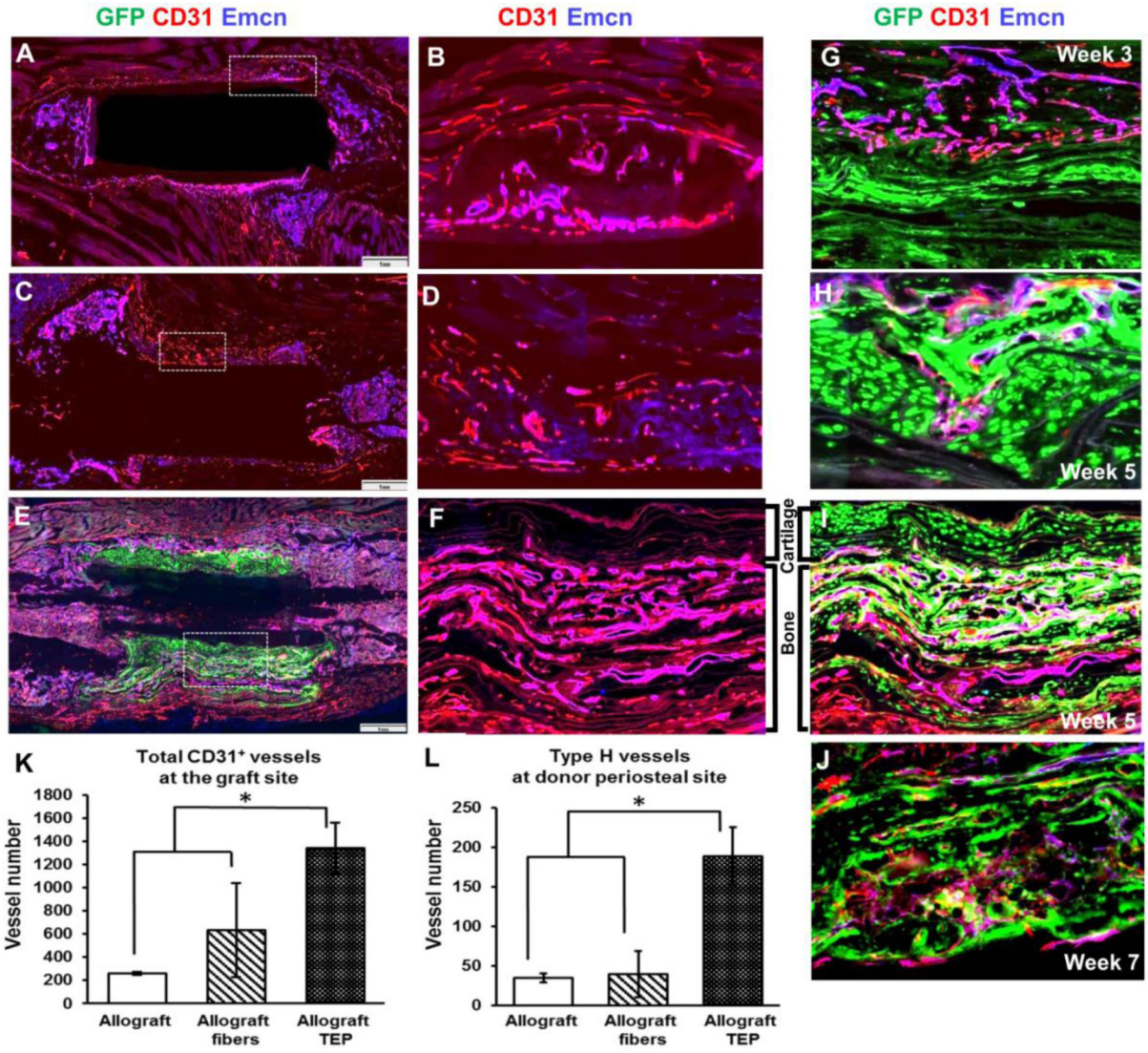

Figure 6. TEP induced type H vessels associated with endochondral bone formation in femoral allograft healing.

Representative overlaying immunofluorescent images of $CD31^{+}$ (red) and $endomucin^{+}$ (blue) vessels in allografts (A&B), allograft with fibers (C&D) and allograft with TEP (E&F) at week 5. Scale bar=1mm. Higher magnification of box regions (5x) show $CD31^{high}Emcn^{high}$ (magenta) and $CD31^{high}Emcn^{null}$ (red) vessels in allograft callus (B), fibrotic tissue (D) and TEP callus (F), respectively. Note that TEP induced new bone-associated multilayered $CD31^{high}Emcn^{high}$ (magenta) and $CD31^{high}Emcn^{null}$ (red) vessels in donor periosteal callus (F&I). Higher magnification images show progressive invasion of these two types of vessels in donor derived bone/cartilage at week 3 (G), 5 (H and I) and 7 (J). Semi-quantitative analyses of the $CD31^{+}$ blood vessels in the total callus (K) and the $CD31^{high}Emcn^{high}$ type H vessels in donor site periosteal callus (L). n=4, $p<0.05$.

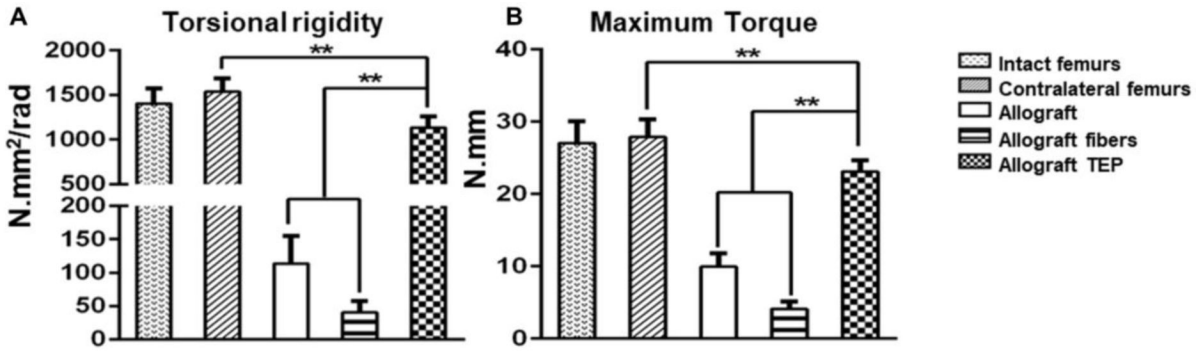

Figure 7. TEP restored inferior biomechanical property of allograft healing.

Torsional rigidity (A) and maximum torque (B) in all three indicated groups of allografts as opposed to intact femurs from non-surgical animals and contralateral femurs of the surgical animals. (n=6, ** $p<0.01$).